The International Journal of Advanced Manufacturing Technology
https://doi.org/10.1007/s00170-025-16354-5

ORIGINAL ARTICLE

Framework for automated measurement of material deposition in welding and directed energy deposition

Carlos Zhu[1,2] · Trayana Tankova[3] · Amin S. Azar[4] · Ricardo Branco[2] · Luís Simões da Silva[1]

Received: 1 April 2025 / Accepted: 5 August 2025

Abstract
Robotic welding and additive manufacturing (AM) processes have an intricate design space influenced by numerous configurable process parameters. Currently, the precise impact of each parameter or a combination of them on the variability and dimensions of deposited material is unclear due to the stochastic nature of the process, which is affected by factors like arc stability, temperature gradients and other in-process changes. In AM and various cases of welding like cladding, quantifying these variations is necessary for developing path planning strategies that produce components without defects. This study presents a framework that automates process data collection and scanning of the weld bead and analysis of the point cloud, based on the design of experiments principals towards building representative machine learning models. In comparison to alternative approaches, this framework incorporates spatial variation along the deposited length by utilising location-based binning of measurements, thereby enabling more detailed analysis of various deposition stages including arc ignition and extinction regions. The framework is tested with single pass bead-on-plate weld beads deposited with different process parameters followed by spatial–temporal matching. Variations were noted in relation to travel speed and welding current when subjected to identical heat input values. Machine learning models for prediction of height and width account for non-linearities and are validated with additional experimental data. These models have demonstrated a high degree of accuracy in predicting in-process variations within the deposited material.

Keywords Welding · Directed energy deposition (DED) · Laser profilometry · Point cloud · Machine learning (ML)

Abbreviations

AM	Additive manufacturing
ANN	Artificial neural network
CMT	Cold metal transfer
COV	Coefficient of variance
CTWD	Contact to work distance
DBSCAN	Density-based clustering algorithm
DED	Directed energy deposition
GMAW	Gas metal arc welding
GRU	Gated recurrent unit
LBFGS	Limited memory Broyden–Fletcher–Goldfarb–Shanno algorithm
MAPE	Mean absolute percentage error
MIG	Metal inert gas welding
ML	Machine learning
MLP	Multi-layer perceptron
PL	Percentage length
R^2	Coefficient of determinant
RANSAC	Random sample consensus
RMSE	Root mean square error
WAAM	Wire arc additive manufacturing

✉ Carlos Zhu
carlos.zhu@uc.pt

[1] Department of Civil Engineering, ARISE, ISISE, University of Coimbra, Coimbra, Portugal

[2] Department of Mechanical Engineering, ARISE, CEEMPRE, University of Coimbra, Coimbra, Portugal

[3] Department of Engineering Structures, Delft University of Technology, Delft, Netherlands

[4] 3D-Components AS, Oslo, Norway

1 Introduction

Additive manufacturing (AM) is a compelling solution for highly customized and complex parts for end-use applications [1]. Due to inherent similarities between the directed energy deposition (DED) technology—a subset of additive manufacturing processes—and classical welding, there is a general trend in adapting governing welding standards in AM industry.

Published online: 26 August 2025

However, developing and defining process parameters remains a critical challenge among all these technologies. With a lack of general frameworks [2, 3], benchmarks [4], and guidelines [5] that allow comparative analysis of different parameters in a unified manner, the retained uncertainties impose challenges such as massive workforce requirement, substantial environmental impact, time-consuming, and costly practices as well as slow innovation in materials, resulting in slower adoption of robotised welding and AM.

All established use-cases in welding and DED start with a fine-tuning of process parameters to establish a usable range of combined inputs for manufacturing [6–8]. For this purpose, studies have been conducted to determine the importance of various factors, including heat input, feed rate, travel speed, and dwell time [9]. However, the intricate control systems in modern welding (i.e., synergic processes) and DED machines make the analysis and conclusions on process variability unclear for practical applications, particularly considering the complex interconnection of factors linked to the physical phenomena such as thermal gradients, Marangoni flow, heat dissipation, and phase transformations.

Thus, the aim of this study is to propose and demonstrate a framework to analyse the impact of process parameters on the bead geometric features and dimensions (i.e., height and width). The framework prioritises the efficiency and practicality to quantify and understand process variations in welding and DED processes, employing non-destructive metrology methods and a robust ML (machine learning) method using a deep learning algorithm. To connect these methods, an algorithm streamlines the processing of raw data converting point cloud into metrics for the surface analysis and modelling, and introducing a novel location-based approach to capture the spatial variation of the process.

Lastly, to test and demonstrate the framework, an experimental campaign (considering variations in welding current and travel speed) is conducted for single weld beads using an integrated additive manufacturing system, which consists of a Fronius CMT welding torch powered by a TPS 400i and controlled by an ABB IRB-4600 robot and a RobTrack system [10]. A seam tracking sensor operating in profilometry mode, controlled by a dedicated in-house developed software that collects and analyses the streamed data from the welding machine, robot and sensor. All components are fully integrated into the robotic DED cell to capture the single weld-bead characteristics.

2 Background

2.1 Process parameters as "factors"

Modern welding machines offer numerous internal and external parameters for process adjustment. Internal parameters include those set within the machine, such as wire feed rate, welding current and voltage, shielding gas flow rate, and frequencies. External parameters are related to material physics or robot configuration, including torch travel speed, inter-pass temperature, cooling rate, contact-tip-to-work distance (CTWD), wire diameter, torch angle, pre-heat temperature, substrate thickness, substrate material and preparation, wire consumable, and shielding gas compositions.

In traditional gas metal arc welding (GMAW), key factors affecting microstructure and bead shape are heat input and energy density [11], which are widely employed in industries to assess weld quality. A significant issue with heat input is that its components (current, voltage, travel speed, and efficiency) can be varied in different ways to achieve the same heat input value, yet their impact on bead geometry differs substantially [12, 13]. The ratio between the wire feed rate and travel speed is another factor that affects the bead shape, as there is a phenomenon known as humping effect, which is a consequence of an incorrect combination of travel speed and wire feed rate leading to material accumulation [14].

Concerning the substrate, Gudur et al. [15] observed how the initial temperature (pre-heat) can alter the bead geometry of Inconel 625 consumable, with an increase of width and penetration depth and decrease of height when pre-heated to 500 °C. Ščetinec et al. [16] showed that CTWD and electrical current have a nearly linear relationship, and Almeida [17] confirmed their effect on bead geometry.

The studies clearly show that identifying ideal conditions can be ultimately complex. Additionally, there is a noticeable lack of agreement on the classification, ranking, and sensitivity to variations of these factors on the measured bead profile, with limited discussion on repeatability.

2.2 Deposited bead morphology and dimensions as "responses"

A single deposited bead forms the fundamental unit of the layering process in directed energy deposition technology. Optimal defect free deposition strategies considering multiple beads and multiple layers are based on quantifying the deposited bead via its cross-section dimensions. Figure 1 illustrates the main geometrical features of a single weld bead, namely: width (W), reinforcement height (H), penetration depth (D), toe angle (θ), reinforcement area (A_D), and dilution area (A_S).

2.3 Correlation between factors and responses

In many instances, data-driven methods are utilised to forecast these characteristics. Chan et al. [19] reported the use of backpropagation neural network models to predict variables such as bead width, bead height, penetration depth,

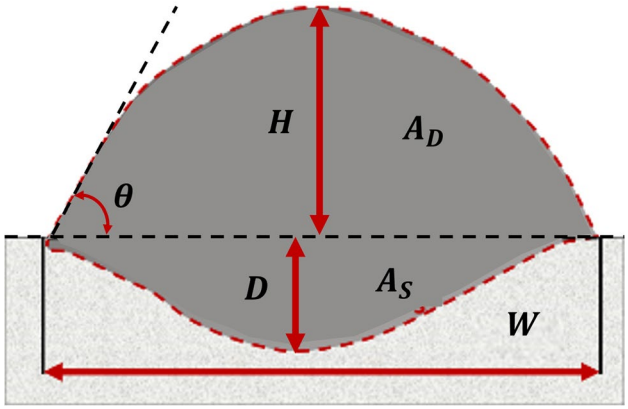

Fig. 1 Measurements of a weld bead profile, adapted from [18]

reinforcement area, dilution area, and a parameter dubbed bay angle and length.

Similarly, Xiong et al. [20] compared neural network and second-order polynomial regression models for weld cross-section profiles, concluding that the neural network model outperformed due to its superior capability to approximate non-linearities. Likewise, Nalajam et al. [21] investigated forward and backward propagation neural networks to model the weld bead dimensions using process parameters for CMT welding, obtaining a dataset by cross-sectioning each weld bead in a transversal direction and conducting a macrostructural examination to obtain the measurements.

While most works focus on straight line deposition paths, Petrik et al. [22] developed an algorithm for 3D reconstruction of curved paths that takes the welding trajectory into account. Their approach yielded relevant results in path planning by considering the radii of curved paths and analysing both multi-layer perceptron (MLP) and gated recurrent unit (GRU) models. They found similar convergence for the predictions when locations in the weld were represented as a 4D vector input in the MLP model. In addition, Petrik et al. [22] show a predominance of neural networks with MLP architecture.

Advancements have focused on modelling bead-on-bead interactions [23, 24] and on the use of artificial intelligence methods for inspection and process control [25]. These studies demonstrate progress in linking factors and responses, yet often overlook variations along the deposition length, and have unclear methods from data gathering to model development. Thus, the proposed framework provides a systematisation of data collection, analysis, and modelling, enabling further studies like defect detection and evaluation of the dimensional variability of stacked beads due to changes of the shape of the underlying material and variations on specific weld locations/paths. In contrast to the work conducted by Lettori et al. [26] that focuses on 3D scanning and data segmentation to evaluate the deposited geometry, the present work contributes a novel perspective by demonstrating the potential for automation using in situ laser profilometry and incorporating point cloud segmentation and machine learning for deeper analysis.

3 Research methodology

From a wholistic perspective, the proposed framework in this study involves (i) an algorithm that processes surface data (point cloud) collected through a laser profilometer, (ii) a design of experiments to replicate various factor combinations and gather data in a controlled and statistically significant manner, (iii) modelling of the relation between factors and responses, and (iv) a validation test dataset to verify results. For this study, these constituents are configured towards the analysis of bead-on-plate samples produced with CMT-GMAW and modelled with ML methods. They are defined as follows:

- **Algorithm**: An algorithm is defined to convert 3D point cloud into response metrics such as bead heights and widths along the deposition path;
- **Experimental procedure**: An experimental campaign is undertaken using the CMT-GMAW process, covering a range of selected process parameters (in this case travel speed and welding current). For each weld bead, a point cloud of the surface after welding is obtained through laser profilometry. Additionally, for comparison, manual measurements with a digital calliper and with Fronius WireSense technology [27] are performed;
- **Regression models**: A multi-layered perceptron neural network predicts weld bead dimensions (height and width). These predictions are validated by recreating the weld bead surface geometry and comparing it with actual measurements from a laser profilometer using an independent validation test set.

4 Algorithm for object detection and point cloud analysis

The algorithm comprises a sequence of steps that transforms data points from a Cartesian three-dimensional space into metrics for evaluating geometry. Figure 2 provides a summary of the algorithm that is subsequently described, considering the following assumptions:

(a) The object being evaluated is unknown;
(b) The point cloud data is uniformly distributed in space;
(c) Multiple objects might be present for evaluation;
(d) At least one reference can be identified within the point cloud (in this case, the substrate plane);

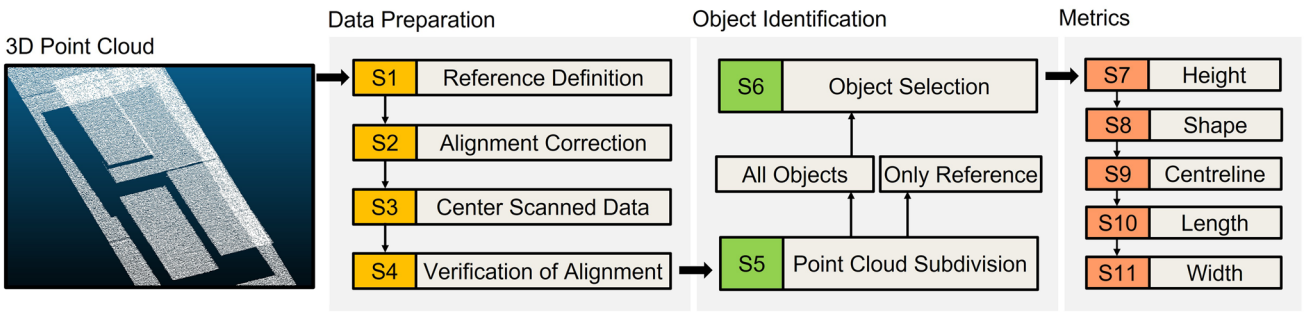

Fig. 2 Flow chart explaining the implemented point cloud processing algorithm. "S" stands for step

(e) Noise or outliers may exist.

Assumptions (a), (c), and (e) suggest that the algorithm is adaptable for analysing various geometries beyond the specific case of single weld beads, whereas assumptions (b) and (d) limit its broader applicability. Overcoming assumption (b) has two solutions, one is to simply find a stable data/scanning acquisition rate according to the travel speed used. If not possible, data pre-processing methods such as those discussed by Prasad et al. [28] can be used. More concerning is assumption (d), because there can be cases where the substrate plate is not within the raw point cloud data (e.g., in multiple layers deposited). To address this problem, some pre-processing is proposed in step 1.

Step 1: This step involves defining a reference for the measurements, which is considered as a plane equation mapping the surface on which objects are positioned (such as a table, a flat metal plate, or the substrate). The following scenarios can be considered:
First, when no reference can be identified in the raw point cloud data, an external calibration of the reference plane can be considered. For example, the robot cell can be placed on three reference points on the base material, and the relative position of these points can be used to calculate the plane equation. Then, knowing the relative position of the scanning equipment and the deposition equipment allows to calculate the relative position of the point cloud.
The second case involves considering non-flat references (e.g., welding on a curved surface). In this scenario, prior scanning of the surface before welding can serve as a ground truth by calculating the relative distance to an imposed reference plane (as done in the previous scenario). This allows determining a correction matrix for height measurements that is added to measurements obtained in step 7.
The third scenario assumes that a flat reference can be found in the raw data, allowing the automatic determination of the plane equation by using the random sample consensus (RANSAC) method [29]. This technique attempts to fit a model (i.e., a plane equation) on subsamples of the entire data set, where each iteration provides a chance to discover the optimal model. The RANSAC method is characterised by the number of data points in each subsample, the number of iterations it undergoes, and the cut-off distance (distance threshold) for accepting points into the fitted model. For this application, each subsample includes the minimum number of points required to define a plane (three points), followed by 1000 iterations with an assumed distance threshold of 0.5 mm. The resulting plane equation follows the notation in Eq. (1), where a, b, c, and d are the calculated plane coefficients. In this case, the central point of the plane is not considered because it is not required for height and width measurements:

$$ax + by + cz + d = 0 \tag{1}$$

Step 2: Without information on how the point cloud was obtained, misalignments between the scanning device and the object may occur, as shown in Fig. 3. This step involves verifying and correcting these alignments, particularly along the x-axis (R_x) and y-axis (R_y), by calculating the relative angle between the plane normal (step 1) and the Cartesian axis, calculating the intrinsic rotations. The intrinsic rotations are computed following the xyz convention, as demonstrated in Eqs. (2), (3), and (4), where (P_x, P_y, P_z) is the original point from the point cloud, and (NP_x, NP_y, NP_z) is the aligned point;

$$R_x = -\left(\frac{\pi}{2} - \left|\tan^{-1}\left(\frac{c}{a}\right)\right|\right) \times \left(\frac{\tan^{-1}\left(\frac{c}{a}\right)}{\left|\tan^{-1}\left(\frac{c}{a}\right)\right|}\right) \tag{2}$$

$$\mathrm{R_y} = \left(\frac{\pi}{2} - \left|\tan^{-1}\left(\frac{\mathrm{b}}{\mathrm{a}}\right)\right|\right) \times \left(\frac{\tan^{-1}\left(\frac{\mathrm{b}}{\mathrm{a}}\right)}{\left|\tan^{-1}\left(\frac{\mathrm{b}}{\mathrm{a}}\right)\right|}\right) \tag{3}$$

$$\begin{bmatrix} NP_x \\ NP_y \\ NP_z \end{bmatrix} = \begin{bmatrix} \cos R_y & 0 & \sin R_y \\ 0 & 1 & 0 \\ -\sin R_y & 0 & \cos R_y \end{bmatrix} \begin{bmatrix} 1 & 0 & 0 \\ 0 & \cos R_x & -\sin R_x \\ 0 & \sin R_x & \cos R_x \end{bmatrix} \begin{bmatrix} 1 & 0 & 0 \\ 0 & 1 & 0 \\ 0 & 0 & 1 \end{bmatrix} \begin{bmatrix} P_x \\ P_y \\ P_z \end{bmatrix} \tag{4}$$

Step 3: This step is optional but simplifies the analysis. In this step, the point cloud is translated such that the volume of data is aligned with the x- and y-axis, placing the y-axis at the centre of the point cloud volume, and setting the minimum x value to zero. This can be done with Eq. (5) where (TP_x, TP_y, TP_z) is the point translated and $(NP_{x_i}, NP_{y_i}, NP_{z_i})$ is one of the points that was aligned in Step 2;

Step 4: This step verifies that the reference plane is parallel to the xy plane (normal = (0,0,1)) by recalculating the plane equation for the corrected point cloud obtained in step 3. Ideally, the plane should be represented with $d = 0$, but due to a 0.5 mm threshold distance, d is non-zero, indicating a systematic bias. To correct this error, the correction factor (CF) is calculated as the difference between the mean z-coordinate of the points in the plane and d, as defined in Eq. (5);

$$\begin{bmatrix} TP_x \\ TP_y \\ TP_z \end{bmatrix} = \begin{bmatrix} NP_x \\ NP_y \\ NP_z \end{bmatrix} - \begin{bmatrix} \min_i NP_{x_i} \\ \frac{\max_i NP_{y_i} + \min_i NP_{y_i}}{2} \\ CF \end{bmatrix} \tag{5}$$

Step 5: The point cloud is divided into reference plane points and non-reference plane points, with the latter potentially representing objects or features, as seen in Fig. 5;

Step 6: Involves identifying these objects using the DBSCAN clustering algorithm [30], which relies on two parameters: EPS (distance to neighbours) and the minimum number of points in a cluster. To determine these values, a 4-distance graph is plotted to show the distance of the 4th neighbour for each data point (Fig. 4);

For most data points, the EPS is below 30 when considering a single bead. Thus, the clustering algorithm uses

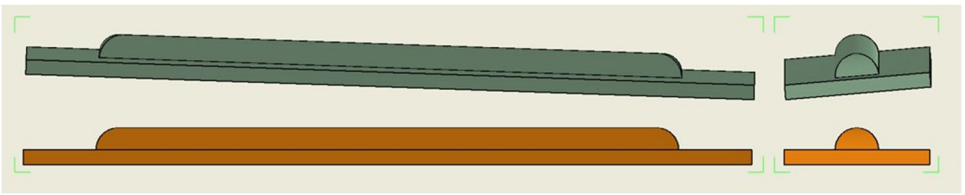

Fig. 3 Illustration of misalignments in scanned data that need to be corrected via step 2 of the algorithm

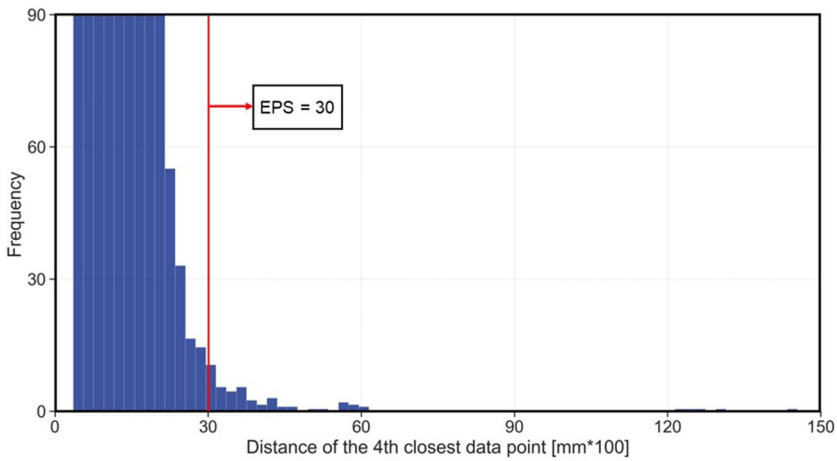

Fig. 4 Selection of EPS parameter by analysing the distance of each data point to the 4th closest data point for one of the weld beads in this case with 5 mm/s (travel speed) and 150 A (current)

Fig. 5 Segmentation of a point cloud into multiple objects, each colour represents an object and/or outliers

an EPS of 30 and a minimum of four points per cluster. When applied to a multi-feature point cloud, it yields a list of clusters as shown in Fig. 5. Additionally, step 6 filters out some outliers based on these parameter values, specifically these are points above the EPS considered.

Finally, steps 7 to 11 involve measuring the object's height (S7), boundary region/polygon (S8), centreline (S9), extreme positions or length (S10), and width (S11):

Step 7: In this step, the data points of the object are projected onto the cartesian *xy* plane by calculating the unit vector of the plane's normal and the distance between each point and the plane. Hence, this distance can be taken as the height of the object, considering the correction factor from step 3 and, if available, the correction matrix from step 1. Accordingly, data filtering can be done: filtering by the maximum value in the transversal direction provides the longitudinal height variation of the sample, while filtering by a specific cross-section reveals the variation at that cross-section. In this algorithm, filtering is done in step 11 to apply the binning concept explained in Section 5.2.

Step 8: The Alpha Shape Toolbox [31] is utilized to derive the bounding polygon of the flattened point cloud, defining the edges with straight lines rather than arcs (alpha shape). For the geometries tested, an alpha value ranging from 0.001 to 0.01 was sufficient to achieve precise representation, although adjustments may be necessary depending on the geometry;

Step 9: In this step, the centreline of the projected point cloud is established using the linear regression method to find the orientation of the scanned object. The resulting centreline is represented by a line equation. A limitation of using the linear regression is that for non-symmetric objects (in the *y*-axis), the centreline is variable; in such cases, another method must be considered to find the centreline, for example straight skeleton [32] or morphological thinning;

Step 10: In this phase, the goal is to determine the extremities of the scanned object by intersecting the centreline with the bounding polygon and measuring the distance between the outermost points. This distance represents the length of the scanned object;

Step 11: In this step, multiple measurements are established based on the length of the object (step 10). For each measurement, a point on the centreline serves as a reference for drawing a perpendicular line to the centreline, which intersects with the straight lines of the bounding polygon (step 8), as depicted in Fig. 6. Analogous to measuring length, the distance between the farthest points is calculated to determine width measurements. All measurements can be saved as.txt or.csv files for further analysis.

5 Results and analysis

5.1 Experimental procedure

To demonstrate the framework, an experimental campaign was conducted using the set-up illustrated in Fig. 7, which consists of a robotic system as described in the introduction [18]. Single weld lines, each 100 mm in length, were produced on $200 \times 350 \times 10$ mm^3 substrate plates made of S235 structural steel, applying an M20 shielding gas mixture composed of 98% argon and 2% CO_2, similar to the study conducted by Tankova et al. [33].

Initially, a scan of the surface without the weld bead was conducted to define the plane angles and general orientation. Then, for each sample, a single weld bead was deposited on the base plate, with the laser profiler actively acquiring the transversal bead profile at 25 frames/s during deposition. After welding, an additional scan was performed at a slower travel speed of 5 mm/s and same acquisition rate to obtain a more comprehensive and dense point cloud.

For this study, only scans acquired after welding were used for the comparative analysis to guarantee that the same density of points between samples is verified, ensuring comparable data. This method is limited by its reliance on post-weld scanning data, but increasing the data acquisition rate relative to travel speed can address this issue.

Samples are defined in an experimental matrix designed to focus on key process parameters, namely the travel speed and welding current. These process conditions were selected from the perspective of initial fine tuning of process parameters (i.e., using an untested combination of wire and substrate consumables), where the travel speed and welding current or feed rate are predominantly adjusted. The selection of welding current rather than feed rate is connected to the

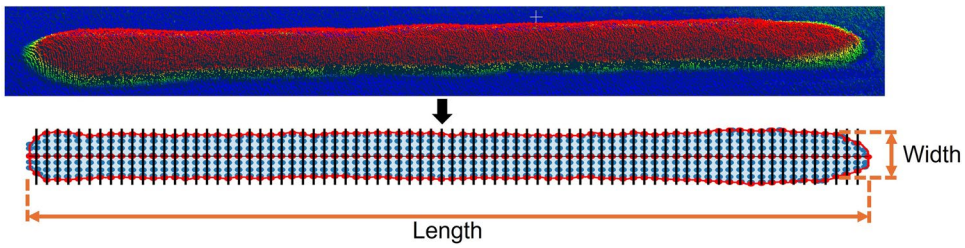

Fig. 6 Measurement of widths and length along the weld bead

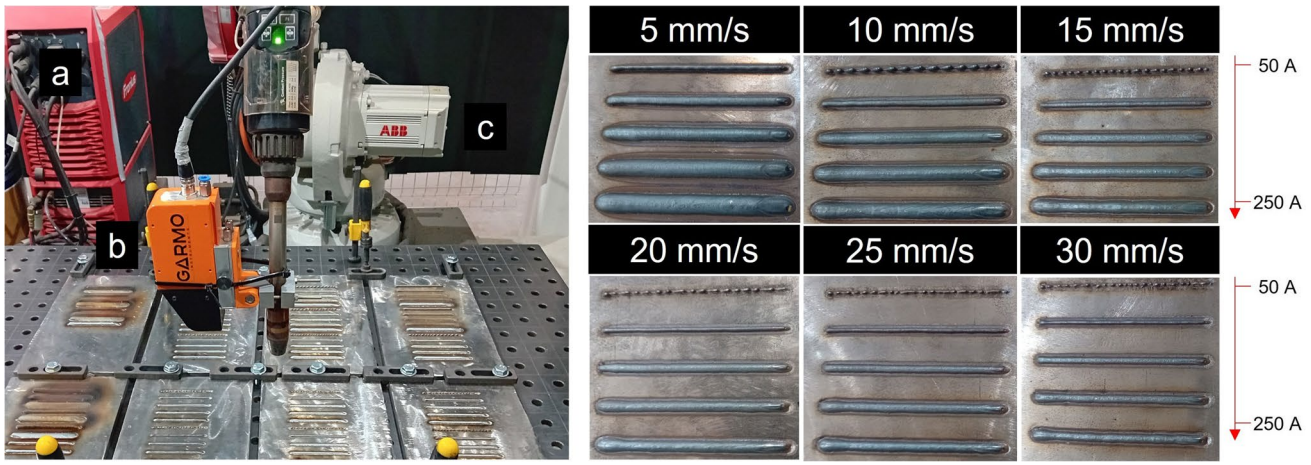

Fig. 7 Experimental layout for WAAM (**a**: Fronius TPS 400i; **b**: GarLine laser profilometer with RobTrack system; **c**: ABB IRB-4600 robot), alongside the initial set of experimental samples WD1

Table 1 Synergic line CMT 3902 universal

Welding current [A]	Welding voltage [V]	Feed rate [m/min]
50	13.2	1.7
100	13.8	3.4
150	15.6	5.8
200	17.3	10.2
250	18.2	13.9

synergic relationship of these parameters in CMT-GMAW, specifically increasing the welding current increases both the welding voltage and feed rate (Table 1). Thus, to avoid codependent variables as input factors, only the welding current was selected due to the direct influence on heat input calculation and geometrical features [34]. Nevertheless, other codependent factors will also change accordingly, and as shown by Catalano et al. [35], they will have particular influence on the outcome of the CMT-GMAW welds in both thin-wall and single bead geometries.

The welding current was examined from 50 to 250 A in increments of 50 A, while the travel speed varied from 5 to 30 mm/s in increments of 5 mm/s. In this way, the welding current is tested in the full range permitted by the welding equipment used for the wire consumable selected with five levels of variation evenly spaced; for the travel speed a broad range is selected to observe the stability and geometrical variation at a set travel speed, in this case again five levels of travel speed are tested. This allows for a square evenly spaced matrix that explores all interactions between levels considered. Although methods like response surface or Taguchi design [36] would reduce the number of specimens needed for accurate prediction, the full factorial approach of evenly-spaced factors was selected to provide a comprehensive view of how process parameters effect on weld bead dimensions in a broad design space.

Due to concerns regarding the impact of plate distortion and variation in inter-pass temperature on sample morphologies (evidenced by Williams et al. [37]), the welds were deposited on six separate plates attached to the workbench. Bead deposition alternated among the plates, allowing each to cool to room temperature before the next weld on the same plate, thus ensuring identical starting conditions and reducing overall experimental time. This strategy ensures a cooling time of at least 60 s between welds. However, this approach introduced two additional issues: (1) calibrating the CTWD; and (2) variability in electrical resistance and inductance of the plates, which can affect welding consistency. The resistance/inductance alignment procedure recommended by Fronius was performed for each plate, resulting in a standard deviation of 0.108 mΩ in resistance and 0.041 μH in inductance. The CTWD was calibrated with an initial stick-out to find the robot's Cartesian coordinates at the point where the wire touches the plate, using Fronius' WireSense technology.

In total, 30 beads were deposited, each representing a combination of process parameter. To evaluate the consistency of the results, each combination was deposited in duplicate, resulting in 60 total samples. These samples are categorized into two data groups: WD1 (weld dataset 1), representing the first set; and WD2 (weld dataset 2) which is a repetition of WD1. Also, samples with the same combination of parameters were deposited on the same plate. Table 1 indicates the specific welding voltage and feed rate associated with each welding current used, and Table 2 lists the parameters that remained unchanged during experiments.

5.2 Data analysis

5.2.1 Data processing

The raw 3D point clouds were processed using the algorithm as described in Section 4. As expected, spatial variation was observed in the material deposition, particularly noticeable at the arc ignition and extinction points (see Fig. 9). Thus, for capturing this spatial variation, a binning concept is proposed, defined by percentage length (PL) parameter.

The percentage length, as the name suggests, quantifies the percentage of the length of the deposited material that is used to determine the average values for height and width within the given segment, similar to a moving average. It is defined by the PL interval that dictates how much of the sample is considered in the calculated averages. For example, if a 10% interval is used, then the "PL bin/value of 15%" represents average measurements between 10 and 20% of the bead length, as shown in Fig. 8b. The percentage representation allows for normalisation of the data that generalises to different lengths and conditions of deposition, based on the hypothesis that there are identifiable regions of variation.

Depending on the PL interval, there are implications on the data analysis. At one extreme, a PL interval of 100% is the average of all the longitudinal variations, while at the other extreme, approaching to 0%, it is the input point cloud data variation. In between, the resulting curves show different levels of variability. Like the concept of surface roughness, a higher PL interval represents the overall waviness smoothing of variations in successive measurements, while a low PL interval tends to capture finer local variations. As visible in Fig. 8a, where "PL interval 1%" (in blue) highlights many instantaneous variations, and "PL interval 20%" (in green) is closer to a flat curve.

This means that it important to define a PL interval in accordance with the specific application. If the objective is to identify local instabilities/anomalies, a lower PL interval is preferable. On the contrary, for modelling general material deposition behaviour, a higher PL interval is preferred, because local and instantaneous variations can constitute noise in the training data.

For the present study, the later was the focus. Therefore, a higher interval of 10% was chosen for testing the framework. This decision was particularly relevant considering that the

Table 2 Fixed parameters for deposition of DoE samples

Parameter	Shielding gas flow [l/min]	Stick-out [mm]	Pistol angle [°]	Synergic line
Value	15	15	90	CMT 3902 Universal

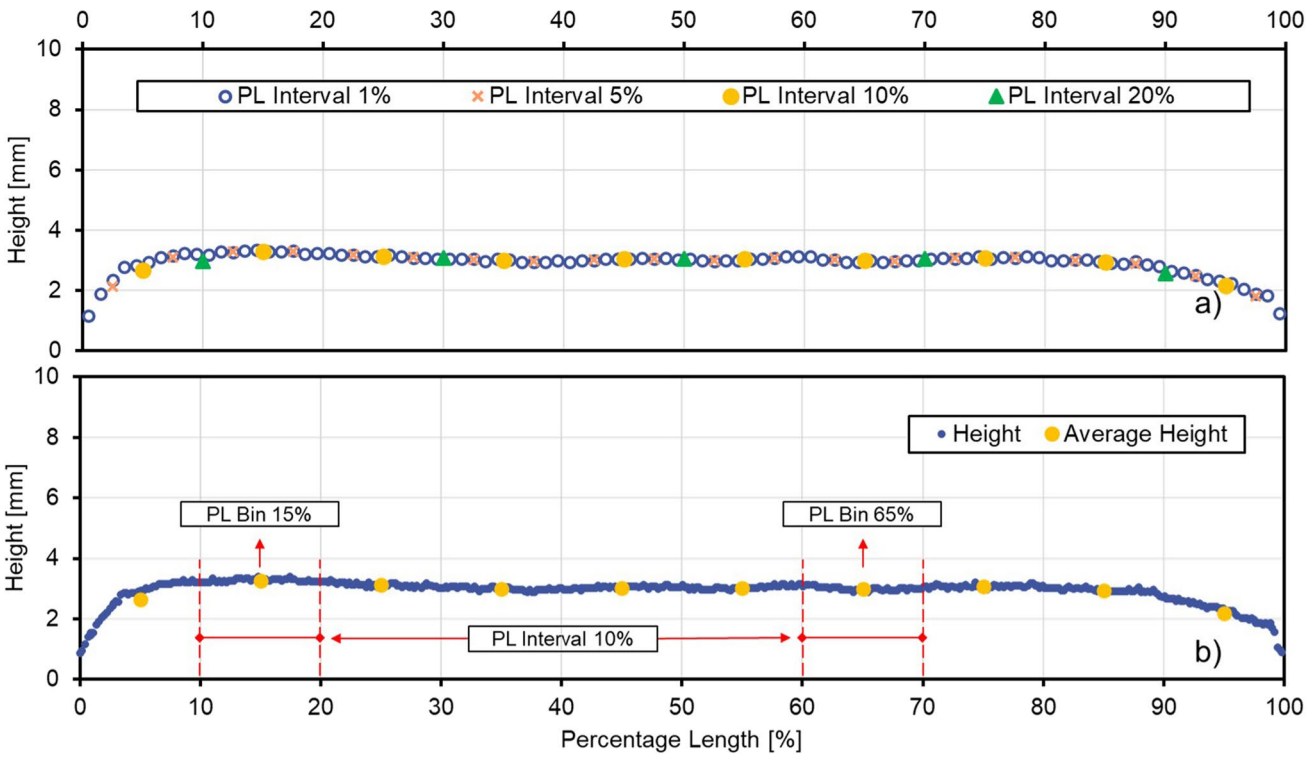

Fig. 8 **a** Effect of different PL intervals on surface variability representation, and **b** example of the measured height profile obtained with the laser profilometer, overlayed with the average height in each discrete interval, in this case segmented by intervals of 10% of PL

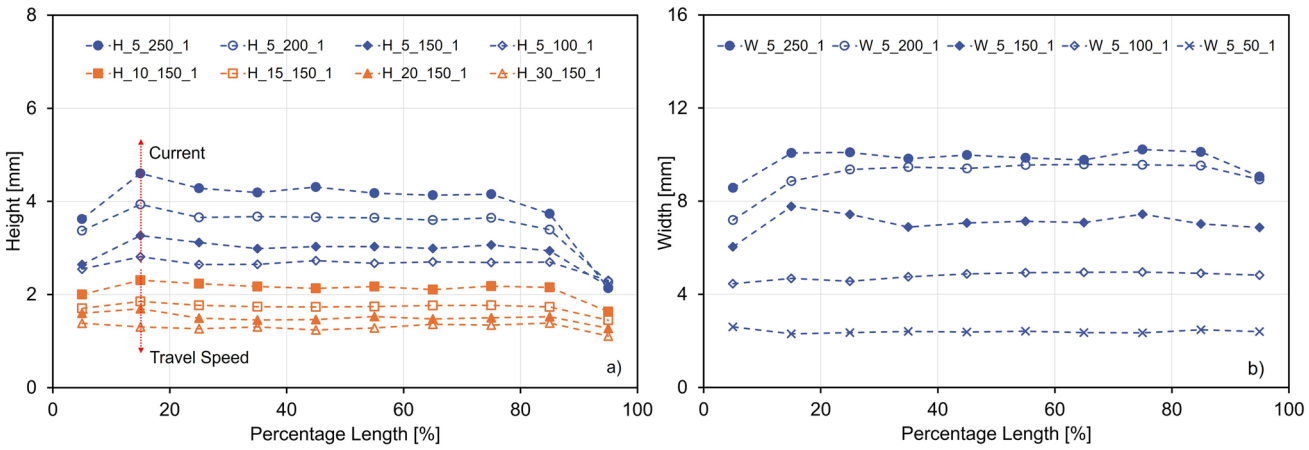

Fig. 9 Weld bead longitudinal profiles for samples in WD1 dataset: **a** height and **b** width

weld beads were deposited without defining ramp-up and ramp-down controls, with start and end currents set to 100% of the main process current setpoint by default. However, for applications that aim to generalise and enhance model predictions in the arc ignition and arc extinction regions, a refined PL interval or dynamic PL strategy is suggested, for example, using PL interval of 5% in the arc ignition and extinction regions and PL interval of 10% elsewhere.

5.2.2 Height and width measurements

Figure 9 shows the progression of height (Fig. 9a) and width (Fig. 9b) measurements from 5 to 95% and depicts typical weld profiles observed during the experimental trials, not all weld beads are displayed to highlight differences in shape associated to variations of current and travel speed. By grasping these variations in cross-section dimensions, an improved tool path planning in DED can be attained. Additionally, identifying the sources of these variations assists users in pinpointing and adjusting the key factors to develop reliable location-specific process parameters. The height measurements in Fig. 9a highlights samples with decreasing welding current maintaining the same travel speed (5 mm/s) and also for the same current (150 A) with increasing travel speed (in orange), disregarding the weld bead with a travel speed of 5 mm/s and a welding current of 50 A due to the atypical pattern observed and discussed afterwords. Likewise, Fig. 9b focuses on width variation when increasing welding current with the same travel speed, yet the variation with travel speed is not plotted due to overlapping of measurements that make it difficult to decern the trend in shape variation.

To ensure clarity, each weld bead sample in the upcoming figures and charts follows the notation [*Height or Width*] _ [*Travel Speed*] _ [*Current*]_ [*Repetition/dataset*]. For example, *H_5_250_1* denotes the height for a weld with 5 mm/s travel speed and 250 A welding current from dataset WD1. Typically, the longitudinal weld profile features: (i) an initiation phase where the height and width rise and then fall, peaking at a PL of 15% for the height, (ii) a stable phase where the bead dimensions stay relatively constant, and (iii) an end phase where the height slowly declines towards the end crater, with the width also showing a slight decrease. For height, the variation in the initiation phase becomes more noticeable when increasing the welding current or reducing travel speed. Conversely, at higher speeds, this variation at the initiation region is less pronounced (Fig. 9a).

By examining each PL value using the coefficient of variation (COV) that quantifies the standard deviation relative to the average dimension, the three phases can be better identified as shown in Fig. 10. Looking at the average COV for both width and height measurements, it can be observed that from 25 to 75% the COV does not change significantly (see Fig. 10b). This interval is therefore considered a "stable" phase/region with average COV values of 0.029 for height and 0.021 for width. For other PL values, it is observed a tendency to increase the COV which is highest at the furthest positions, indicating a change in how dimensions vary. Notably, PL bin of 15% corresponds to the peak height in most profiles, and PL bin of 85% shows higher height variability in welds with high current, such as those deposited at 5 mm/s and 250 A, as seen in Fig. 9.

Figure 11 illustrates the average height and width in the stable region. A positive correlation is found between heat input and height and width, indicating that higher welding current or lower travel speed results in increased bead height and width, this correlation is evidenced by a second-degree polynomial fitted line. However, this trend in height variation is not observed in welds with 50 A, particularly the weld with 50 A and 5 mm/s (calculated heat input of 0.132 kJ/mm) has a greater height than another weld with more than twice the heat input. A further study

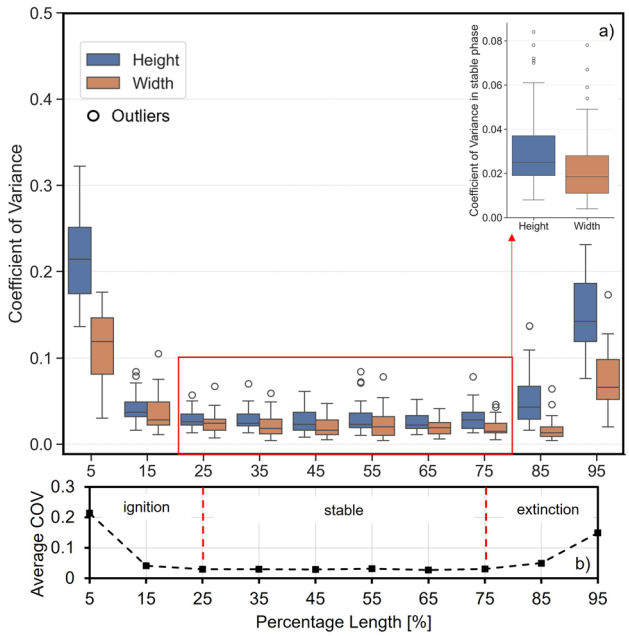

Fig. 10 **a** Coefficient of variation of height and width in each PL bin and **b** average COV value in each PL bin considering width and height of all samples in WD1

is needed to understand this phenomenon. But, one possible explanation is that the variation in bead dimensions is caused by the combination of higher surface tension that prevents the liquid material from spreading laterally due to a faster cooling time and lower dilution (i.e., penetration area, as observed in [17] for CMT-GMAW and [38] for GMAW) associated with lower heat input (welding current and voltage). Therefore, more material accumulates in the melt pool surface which results in a higher deposition height. A similar phenomenon is observed in [39], showing for MIG welding that, depending on the feed rate, a lower heat input can lead to a higher height, supporting the hypothesis of material accumulation.

In both dimensions, a non-linear relationship is observed with the parameters that define heat input (current and travel speed). This analysis excluded welds with 50 A and speeds exceeding 5 mm/s since they showed humping effects. Figure 12a reveals a significant difference in how welding current affects the weld bead height considering a specific travel speed: for example, at travel speeds of 5 mm/s and 15 mm/s, the increase in height due to a higher current is more pronounced at a lower travel speed. The width (Fig. 12b) also displays a non-linear behaviour, where at a fixed travel speed below 200 A, changes in welding current proportionally affect the width. Yet, between 200 and 250 A, the width stays stable. Similar results were found for CMT-GMAW with stainless steel [35], indicating that, in terms of geometrical variations, travel speed and welding current/feed rate should be treated as separate input factors. In addition, these findings also suggest that the CMT-GWAW deposition process exhibits a general trend for the variation of the input factors, but this trend varies depending on the consumable combination used.

5.2.3 Data comparison: variability of process and metrology method

Under ideal conditions, all datasets should have the same dimensions for the same welding conditions; however, this is not observed for the acquired data. This is a well-known problem that makes welding to be considered as a "special process" under ISO 9000 and ISO 3834 standards [40]. Hence, to quantify the difference the mean dimension is calculated considering the specimens produced with the same parameters (WD1, and WD2) at the respective PL bins. Then, the relative difference of each measurement is compared to its mean dimension. Figure 13 exhibits this analysis for width and height. Overall, no observable pattern is found in the scatter of measurements, yet a variation of the measurements is found to be primarily in the range $[-0.2, +0.2]$ mm, which corresponds primarily to a variation below 2% of relative percentage error.

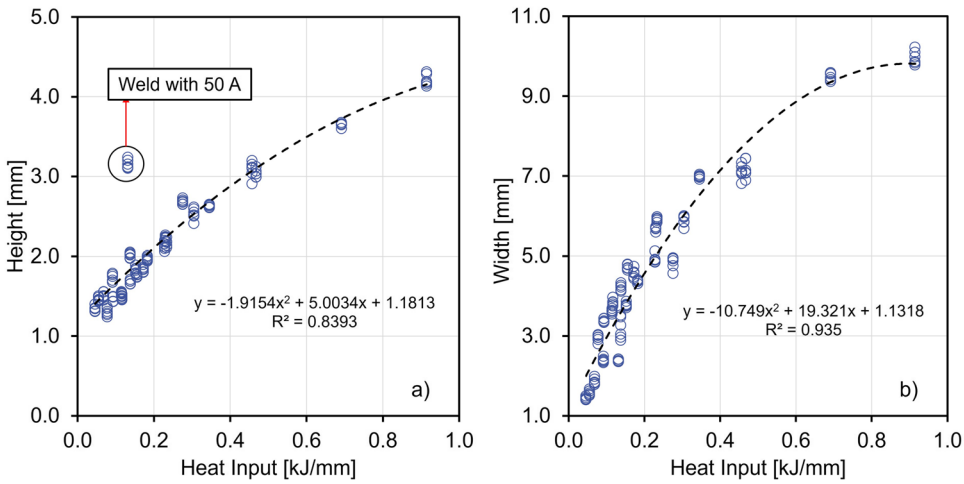

Fig. 11 Comparison of average measurements for WD1 with calculated heat input: **a** height, **b** width

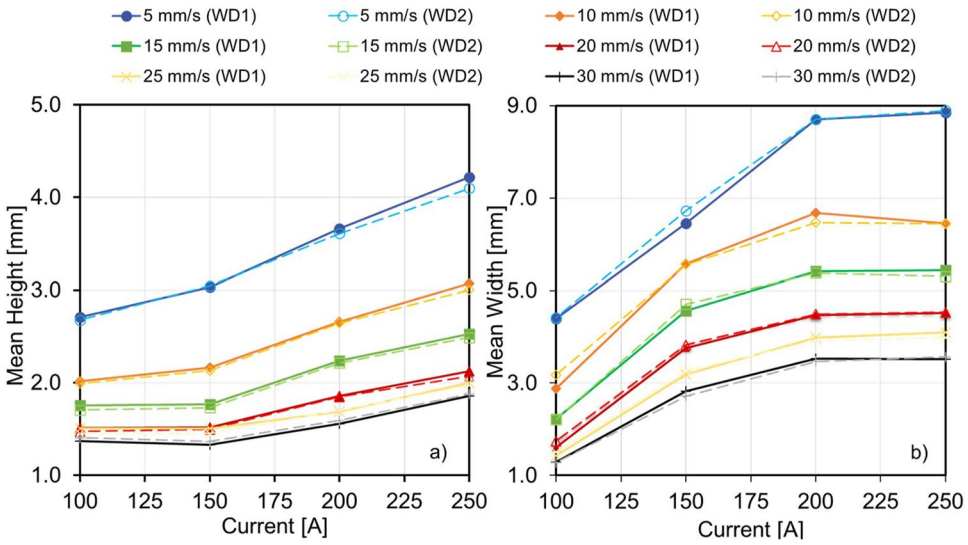

Fig. 12 Effect of welding current and travel speed on weld bead dimension: **a** height and **b** width

Highlighting the variability of measurements, a pooled standard deviation of 0.0805 mm for height and 0.152 mm for width was calculated, when comparing samples produced with the same parameters. This indicates that there is more variability in width than in height. However, comparing the coefficient of variation (COV), the relative error to the mean dimensions is approximately 3.2% for width and 3.9% for height, both below 4%.

Additionally, the accuracy of the measurements obtained through the proposed workflow is compared with other metrology methods, such as digital callipers and Fronius WireSense. To facilitate this comparison, WD1 samples were targeted, allowing for the evaluation of different measurement techniques on identical samples.

Figure 14a confirms that the shapes of measurements taken with the laser profilometer, and the WireSense are similar, despite minor discrepancies in their absolute values. By analysing all measured heights, a correction factor of – 0.4 mm was identified. After applying this factor to all the profilometer measurements, a strong match is observed between the two measurement methods, as shown in Fig. 14b. This demonstrates that both methods can be used to analyse the relative dimensions of the weld bead; because, although there is a difference in the absolute measurement (as indicated by the 0.4 mm correction

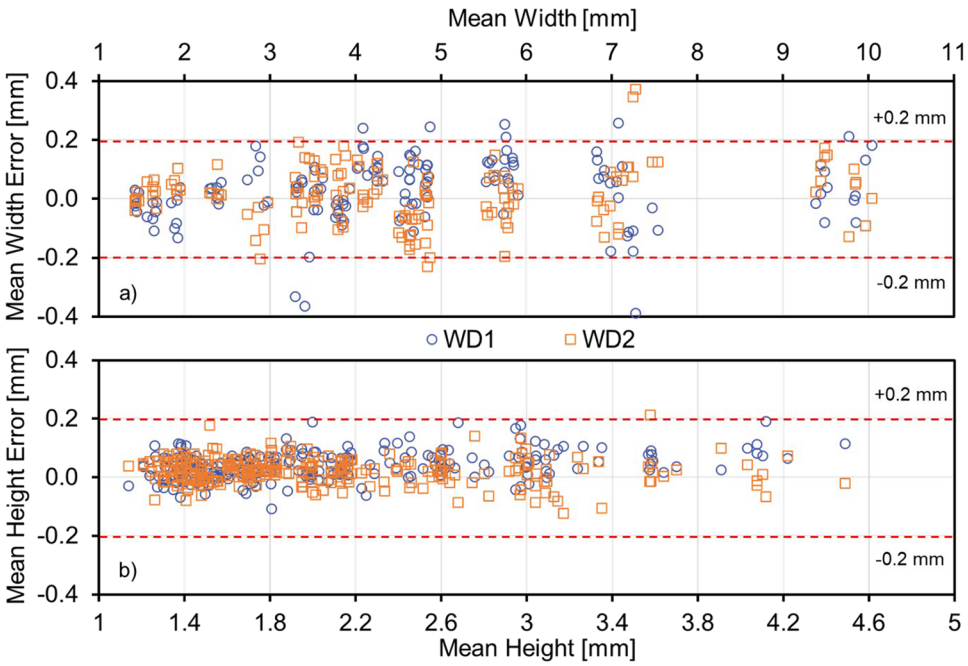

Fig. 13 Relative error to the mean dimensions, for **a** width and **b** height

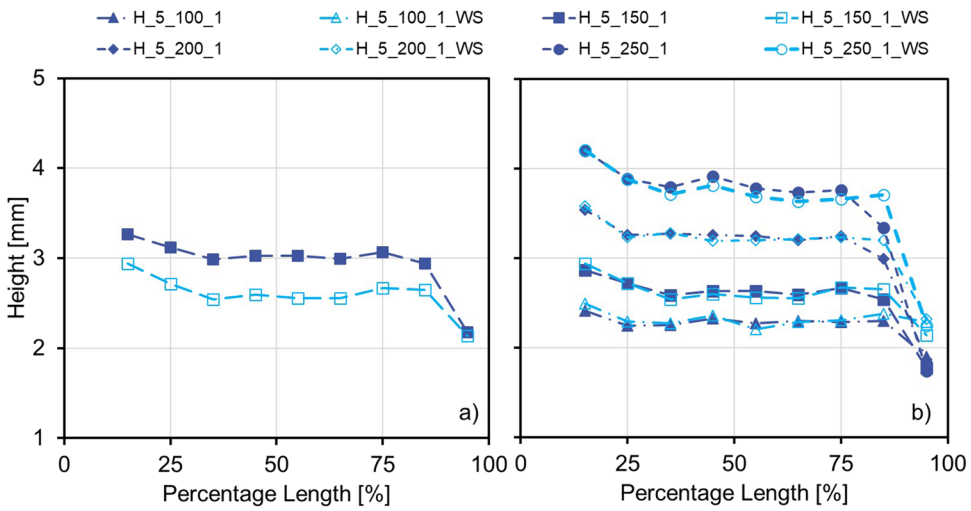

Fig. 14 Comparison between different measurement methods: **a** weld bead deposited with 5 mm/s and 150 A, and **b** when offsetting the height measured with the welding torch by 0.4 mm. Series identified with WS were acquired using Fronius WireSense, while others with a laser profilometer

factor), the relative differences in measurements along the deposited length are nearly identical. Still, it is relevant to note that measurements obtained with laser profilometers require significantly less time.

Figure 15 compares the heights measured by three methods for weld beads at 5 mm/s (WD1) with increasing welding current at PL 55%. All methods show similar trends yet, present 5 to 8% standard deviation in the measured values. More accurate metrology methods, such as macro/microsection analysis, should be used to find the true measurement values.

6 Regression model

6.1 Model development

Since a key objective of this study is to automate and systematize the modelling of the relationship between process conditions and deposited dimensions, a machine learning paradigm is considered since incorporating a model search with a set pipeline makes the framework more flexible and scalable considering other factors and responses/metrics, while providing accurate estimates.

In advanced welding machines, arc ignition and extinguishing phases are usually configured separately and studied independently. However, in this research, the same parameters were used across all samples, allowing data from these regions to be included in ML training and validation. Data with welds that had defects or discontinuities were excluded from the selection; this process was performed manually, but it could be automated using established statistical metrics like standard deviation from the automatically calculated mean values. For each bead, 10 measurement locations along the deposition length were considered, making a total of 250 data points for training the height and

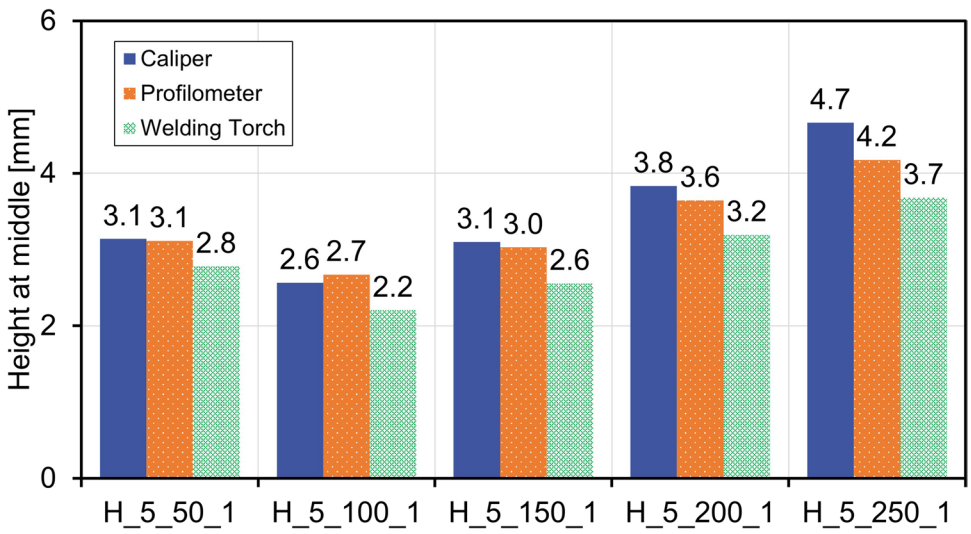

Fig. 15 Comparison of measured height for samples with 5 mm/s and varying current in PL bin 55%

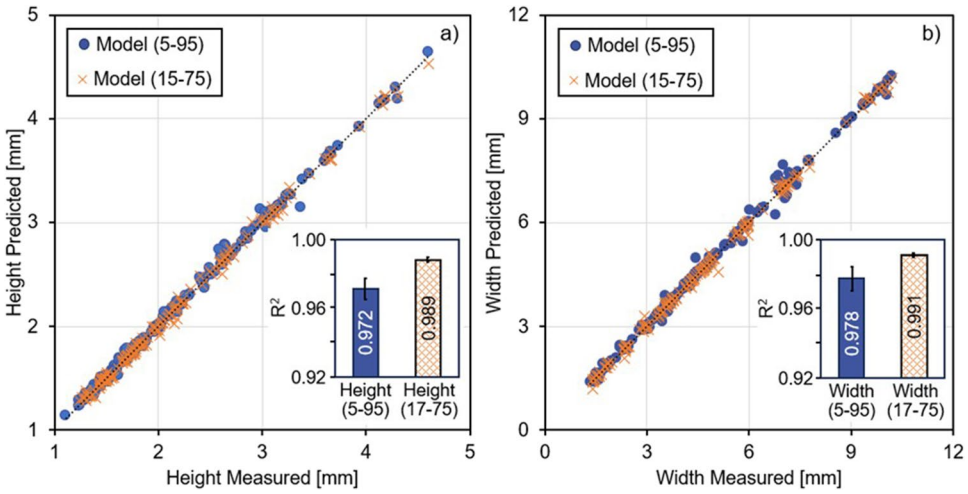

Fig. 16 Comparison between actual measurements and predictions for height and width (WD1), **a** height and **b** width; as well as the corresponding fivefold cross-validations' average $R.^2$ and standard deviation (error bars). Blue represents the full model, and orange represents the model (15–75)

width models. These data points reflect specific segments of the weld bead specimens, influenced by the PL interval used.

Currently, a large PL interval is used to focus on the overall behaviour along the deposited length and to align the predicted bead dimensions with actual measurements. However, using this PL interval reduces prediction accuracy due to variability in the arc ignition and extinguishing regions. Therefore, models of the stable phase (PL between 25 and 75%) with a PL bin of 15% were also trained to capture the peak height and evaluate this loss. These models use welding current, travel speed, and percentage length as factors, while bead height and width are the responses. An artificial neural network (ANN) with multi-layer perceptron architecture is implemented using Python's scikit-learn library.

Prior to training, all factors were normalized to fall within the range [− 1, 1] to standardise them and regularize the parameter search space, thereby enhancing convergence. Next, a multi-layer perceptron model with three hidden layers was trained on 75% of the WD1 data points (selected randomly). The training process involved optimizing the coefficient of determination (R^2) using the limited Memory Broyden–Fletcher–Goldfarb–Shanno (LBFGS) algorithm solver, applying L2 regularisation of 0.00001, utilising the hyperbolic tangent (tanh) activation function for the hidden layers and the identity function as the output function. These were the initial considerations on the tested MLP architecture, defining the other hyperparameters with the default values outlined in scikit-learn library.

Next, a model search is conducted to find the optimum configuration of neurons in each hidden layer looking for highest coefficient of determination. The optimization is done sequentially, where an initial architecture with three hidden layers each with a single neuron is defined. Then, for each hidden layer, a search for the best R^2 value (closest to 1) is conducted, maintaining the number of neurons that give the best fit. The sole limitation is that each hidden layer can have a maximum of 100 nodes and a minimum of 1 node, as a consequence when the best R^2 is found before all hidden layers are optimized then it is possible to have an ANN architecture with single neurons in hidden layers, as seen in Table 3, specifically the width model that considers a PL 15–75% range.

Due to the optimisation, all models present an R^2 for WD1 close to 1 (see Table 3) showing a close estimation of the true values, as seen by comparing the real and the predicted values in Fig. 16a–b. With models presenting a mean absolute percentage error (MAPE) below 1.5% in all models, and a root mean squared error (RMSE) below 0.12 mm for all models, with the largest difference in RMSE observed by comparing the width and height models, where the width models present more than double the RMSE value of the height models considering the same PL bins. This difference in RMSE reflects a higher bias in width measurements that aligns with the uncertainty in the raw data from the experimental samples. The following sources contribute to this uncertainty: (1) the relative

Table 3 Prediction model architecture, considering WD1: R^2 (coefficient of determination), RMSE (root mean square error) in millimetres, MAPE (mean absolute percentage error)

	Hidden layer 1	Hidden layer 2	Hidden layer 3	R^2	RMSE [mm]	MAPE [%]
Width (5–95)	98	43	44	0.9972	0.114	1.2
Height (5–95)	73	99	99	0.9969	0.041	1.4
Width (15–75)	54	1	1	0.9982	0.090	1.4
Height (15–75)	73	53	96	0.9977	0.037	1.3

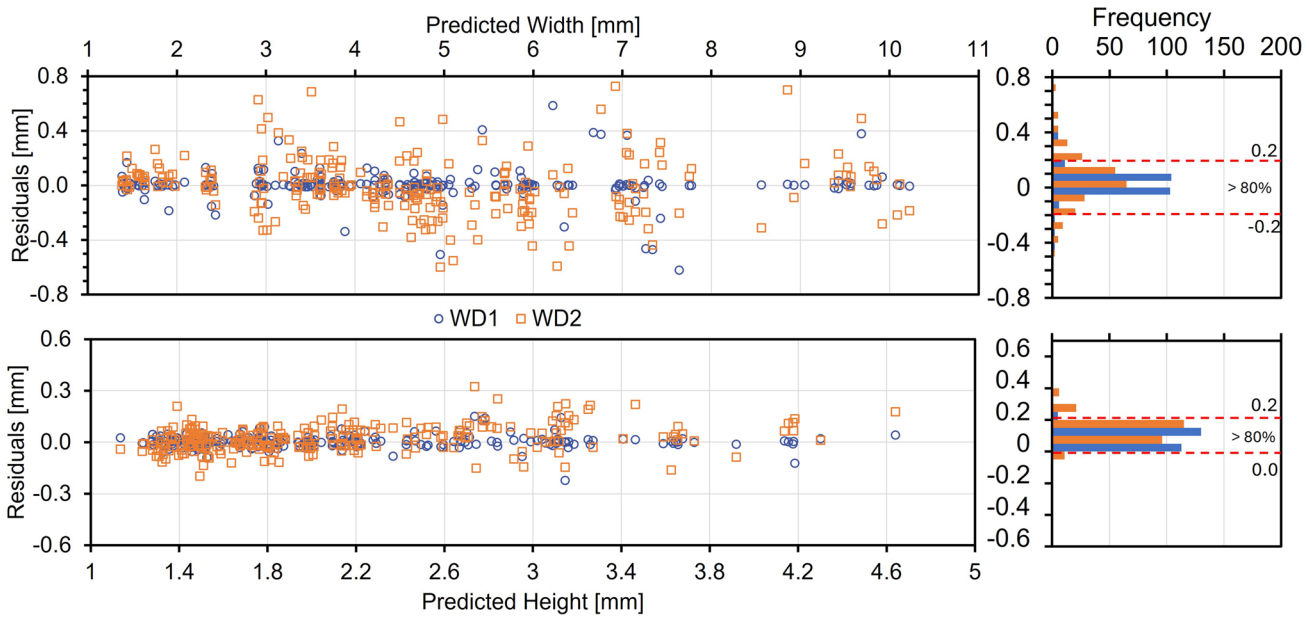

Fig. 17 Residuals of predicted height and width for WD1, and WD2, and the respective distribution of residuals

position of the scanning device to the measured object can introduce higher noise due to the shadow effect and laser distortion; and (2) since the width is proportionally higher than the height, variations and errors in the arc ignition and extinction also have higher impact on width.

The residuals, or the differences between actual and predicted values, are assessed to determine error ranges for specimens WD1, and WD2, and to search for patterns indicating systematic bias. In Fig. 17, height and width errors lack a discernible pattern. This is shown in the testing R^2 scores for height (WD1 = 0.9969, WD2 = 0.9881), which is slightly lower than the training dataset (WD1) but remain within a 1% difference. Similarly, width R^2 scores are WD1 = 0.9972, and WD2 = 0.9899, also within a 1% difference.

Additionally, a fivefold cross-validation was performed by splitting the dataset (WD1) into five distinct training and testing sets, using a 75/25 train/test ratio to access the model's generalisation. Figure 16 displays the average test R^2 and the standard deviation for these test sets. The largest reduction in R^2, about 0.025, is observed in the height model using the full PL range compared to the stable region model. Consistently, models excluding arc ignition and extinguishing phases show better R^2 scores (improved by 1–2%) and less variance (standard deviation of 0.002) compared to full-range models (standard deviation between 0.012 and 0.014). This indicates a trade-off in accounting for the variability of the arc ignition and extinguishing regions, though it is less significant than initially expected. For models characterising these regions, using a smaller PL interval is recommended to gain more data points and better capture the transitions.

These validations show that the modelling strategy is suitable and valid with independent data sources, such as two sets of independent weld beads. However, the predictions must align with physical phenomena, predicting a shape representative of the deposition process. Since this shape varies with current and travel speed, Fig. 18 compares different parameter combinations (used for training) for measured and predicted dimensions (Fig. 18a refers to width, and Fig. 18b refers to height): (i) 5 mm/s and 150 A, (ii) 20 mm/s and 150 A, and (iii) 5 mm/s and 250 A. The bead height generalization is acceptable, with minor discrepancies between actual measurements and predicted values, showing 3–9% error in the mean height of the stable region. Yet, the model is somewhat less accurate in the arc ignition and extinguishing regions for the weld at 5 mm/s and 250 A due to higher transition slopes not captured with the PL interval 10%. Additionally, the predicted and measured widths match the general trends, though with smaller variation in the profilometer data in the predicted data (e.g., in the weld with 5 mm/s and 150 A).

6.2 Model validation

The models demonstrate a good capability to predict the spatial variation of the welding deposition process. However, there remains uncertainty regarding the model's capabilities to generalise to unseen data, due to possible overfitting. To assess the generalisation, the model's learning curves are evaluated. These learning curves are obtained by a cross-validation dataset splitting strategy to define five datasets with different training and testing data points from the original

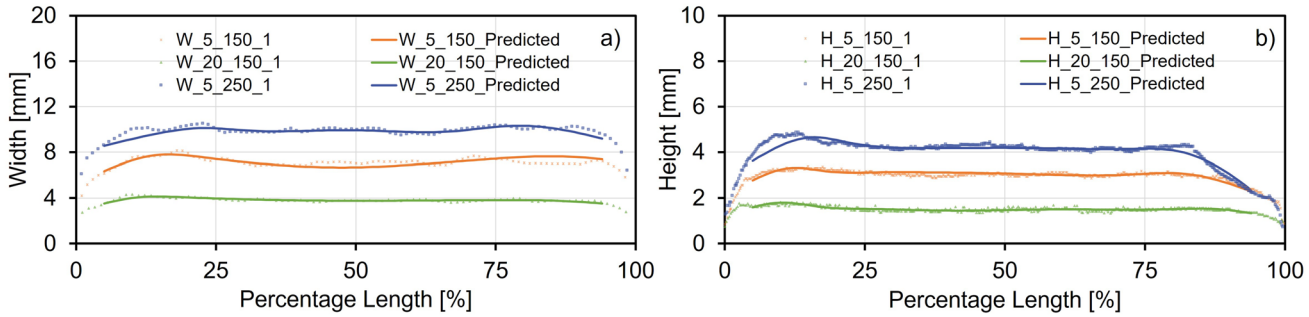

Fig. 18 Comparison of predicted and measured **a** height and **b** width for: (i) 5 mm/s and 150 A, (ii) 20 mm/s and 150 A, and (iii) 5 mm/s and 250 A (WD1)

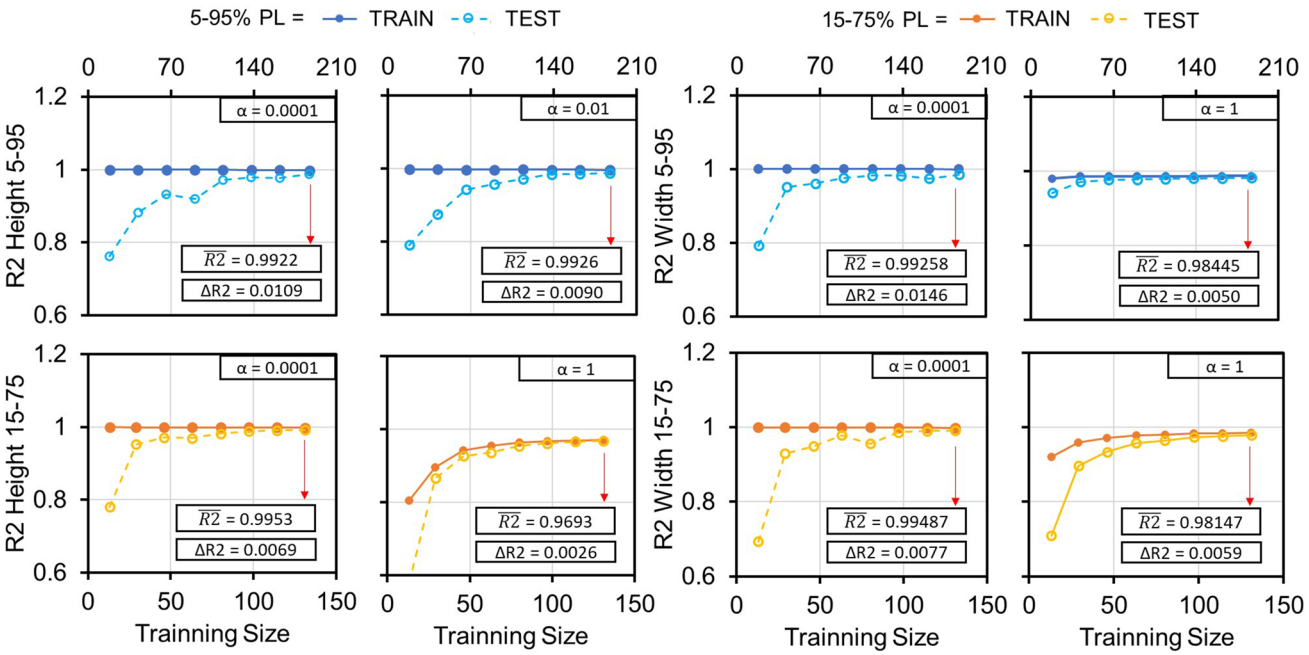

Fig. 19 Learning curves of the models trained using the coefficient of determination as the scoring metric. In blue are the 5-95% PL models, and in orange are the 15-75% PL models

input. In this case, this was done via "ShuffleSplit" function, as done in the fivefold cross-validation in combination with the "learning_curve" function in scikit-learn library to obtain the coefficient of determinant with increasing number of training samples, tested up to a 75% training set size (the same proportion used to define the models).

Figure 19 displays the learning curves for both the width and height models, considering the 5–95% PL range and 15–75% PL range. It also plots the average coefficient of determinant from the fivefold cross-validations. Analysing the originally trained architecture that used very limited L2 regularisation ($\alpha = 0.0001$), it is observed that the accuracy of training datasets remains high even with a limited training size, while the testing accuracy tends to increase converging towards the training accuracy when increasing the training size. This suggests that, with a limited number of samples, the models tend to overfit and, consequently, fail to generalise well the behaviour. However, when enough samples are provided, the model's ability to generalise converges and stabilises.

Based on these learning curves, there is no significant indication of overfitting. Nevertheless, to further verify possible overfitting, learning curves that use the RMSE as the scoring metric are plotted in Fig. 20, to evaluate the error at the scale of the measured dimensions. Thus, in Fig. 20, it is observed that the initial architecture ($\alpha = 0.0001$) does show signs of overfitting when comparing the training and testing curves, which is most critical in the full model (5–95%) for width.

A way to resolve this problem can be to increase the dataset as there is still potential to reduce the variance of the training and testing dataset. Another solution is to apply regularisation techniques (like dropout or L2 regularisation). For this study, the application of L2 regularisation was selected because the Python library used (scikit-learn) does not natively support dropout method, while L2 regularisation is in-build into the MLP pipeline.

The L2 regularisation is applied considering the α parameter, where a higher α means a higher penalisation of the weights of the ML model. Different values of α were tested for the ML models, finding that increasing the α to 1 in the model trained without the arc ignition and extinction (15–75%) demonstrated the best generalisation (see Figs. 19 and 20), although with reduced accuracy. Similarly, the variance of 5–95% models with increased α also led to lower variance. In this case, an α value of 0.01 was used for the height model because α equal to 1 resulted in signs of underfitting.

Overall, the modelling approach considering the MLP architecture has been tested and demonstrated to be a valid approach, achieving high accuracy (high R^2) with a good generalisation, depending on the level regularisation applied. However, further model tunning is necessary particularly considering the uncertainty in the deposited samples (i.e., variations during deposition of material), as this can contribute to the bias found in the models, as observed in the learning curves.

6.3 Model evaluation

This study focuses on evaluating the obtained prediction models rather than refining models with different PL intervals and hyperparameters. The full models (PL 5–95%) were used to observe the complete weld bead length (shape and dimensions). To further validate the models, process parameters which were not considered in the initial study are tested, specifically (i) 12.5 mm/s with 125 A, (ii) 17.5 mm/s with 175 A, (iii) 12.5 mm/s with 225 A, and (iv) 22.5 mm/s with 225 A. These combinations fall within the original experimental matrix, but they were not used for training, making them ideal for testing the model accuracy and generalisation.

Figure 21 a and c compare the predicted height of the weld bead geometries to the measured data from the laser profilometer. Although the trend is similar, the predicted height is generally lower than the actual measurement. In the stable region (PL 25 to 75%), the weld with 125 A and the weld with 225 A are on average 0.092 mm and 0.077 mm, respectively, lower than the measured values (Fig. 21a). The other two welds (Fig. 21c) also underestimate height, in this case approximately by 0.126 mm for 225 A and 22.5 mm/s, and 0.170 mm for 175 A and 17.5 mm/s, in the stable region. More critically the height increase in the initiation region is largely underestimated in the weld with 225 A and 22.5 mm/s.

The width measurements are shown in Fig. 21b and d. It is found that in general the predicted width shows a close

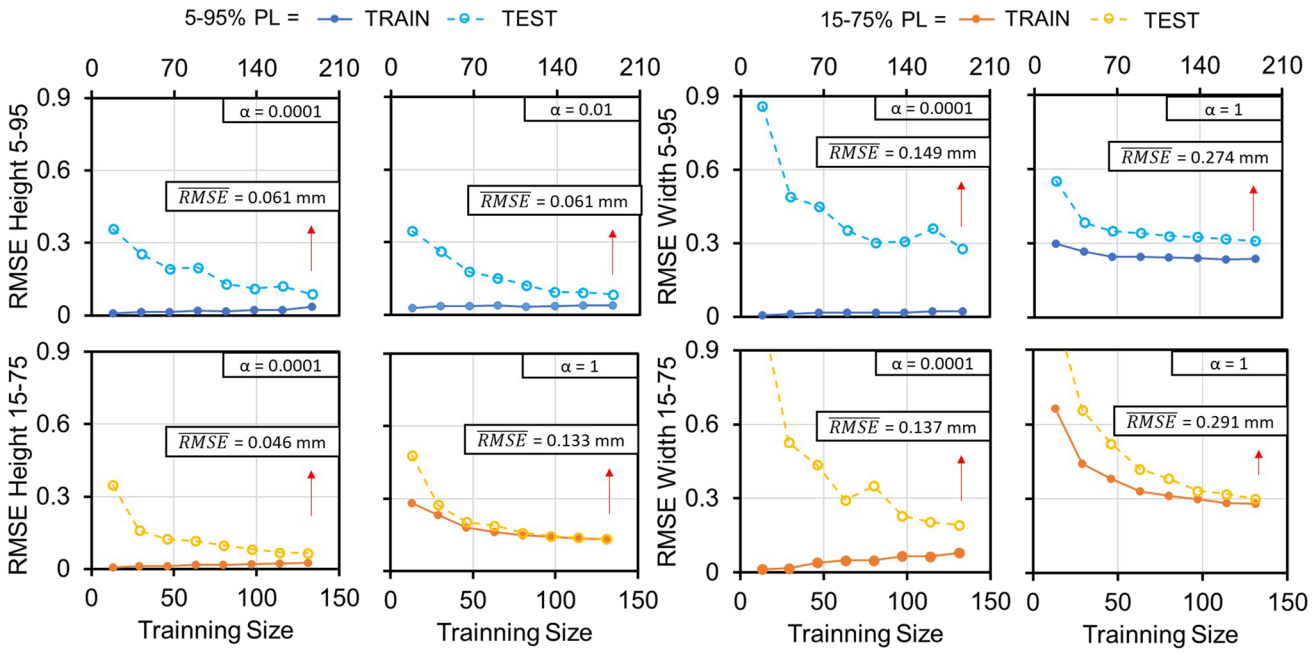

Fig. 20 Learning curves of the models trained using the RMSE as the scoring metric. In blue are the 5–95% PL models, and in orange are the 15–75% PL models

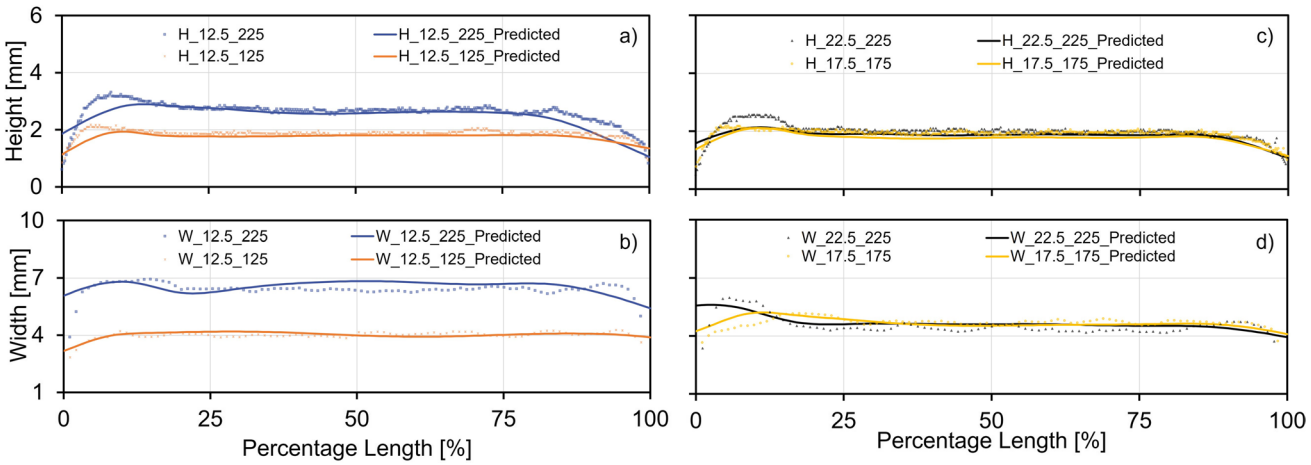

Fig. 21 Comparison of predicted and measured height and width along the length, considering varying travel speed and welding current combinations

approximation to the measured width in terms of evolution, where welds with the same current/travel speed ratio (Fig. 21d) represent different transitions in the arc ignition region caused by the higher amount of material accumulated (humping phenomenon) associated with higher current and, consequently, higher feed speed. However, the weld with 12.5 mm/s and 225 A is visibly different in the stable region, where the prediction overestimates compared to the measured values. This observation is evident when examining Fig. 22 that compares the average measured width with the predicted width in the stable region. The relative error in measurements ranges from 0.5 to 5.2% of the bead width.

Figure 22 compares the measured and predicted mean dimensions (height and width). The poorest prediction was for the weld bead with 22.5 mm/s and 225 A, showing the largest error in width (0.229 mm) and the second largest in height (0.126 mm). Overall, the models provide reasonably accurate predictions within the process variability, yet the fact that with the same pre-defined process parameters there exists an observable variation of dimensions, as evidenced by comparing both datasets, means that improved predictions models that consider the range of deviation of the process itself are required; for this purpose, two suggestions are made for further studies: the first is to incorporate the variations of specific process parameter (e.g. welding current) into the specific weld bead location (PL bins), the other suggestion is to explore more activation functions to fit specific phenomena (i.e., the arc ignition and extinction sections).

In addition, the framework proves to be efficient, because although the computation time was not focused in the study using a standard laptop computer (with an i7-12650H core CPU and a 16 GB of RAM) the model selection of the width and height models (5–95% PL) took approximately 2 h (1 h/model), while running the point cloud processing algorithm took less than 1 min per sample (e.g., 33 s for one of the samples); which considering the samples' deposition and scanning time (e.g., cooling of at least 1 min) means that the data acquisition and processing are close to real-time.

7 Conclusions

The present work contributes to the systematization and generalization of the welding and DED processes measurement and geometrical analysis, introducing a framework/methodology for this purpose. This approach collects and matches temporal data from robotic welding and DED setup and spatial data from a non-contact linear laser profilometer. Additionally, an advanced ML algorithm was proposed and validated towards accurate prediction of the weld bead height and width or defining the process parameters based on the expected bead shape design values. The study examined 30 different combinations of welding current and travel speed, covering a broad range of CMT-GMAW parameters. The main conclusions are summarized below:

- The automatic measurement algorithm for 3D point clouds proved to be an effective way to systematize the measurement process. It was designed to detail the essential steps for assessing geometrical data with minimal assumptions.
- To better capture weld bead variability, the weld was divided into segments and an averaging technique was applied. By examining the coefficient of variation within each segment the weld bead is categorized into arc ignition, stable, and extinguishing regions. It was determined

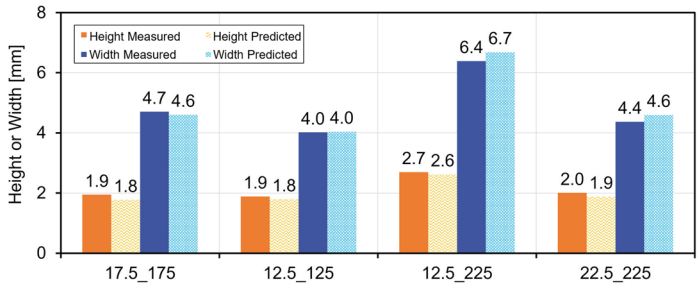

Fig. 22 Comparison of average dimensions with predicted dimensions in PL 25% and 75%

that the stable region encompasses between 25% and 75% of the analysed sample, i.e., single line weld beads.

- The framework applies multi-layer perceptron method to developed and establish the process window. Each node assigns hyperbolic tangent activation function and performs a model search for optimising the number of perceptrons based on the R^2 performance metric.
- The predicted weld bead dimensions shows acceptable accuracy for process parameters tested outside the original design matrix, as demonstrated by comparing extrapolated results where the prediction errors (i.e., the differences between predicted and real values) are found within the range of variations observed in replicated samples. In addition, the spatial variation patterns are similar to those observed in the real samples. Still, the model's prediction of the weld geometry at the arc ignition and extinguishing regions were somewhat compromised due to the coarse PL interval (10%) used.

Through the experimental campaign, the robustness of the framework has been demonstrated. Future work will focus on building models that combine the effect of more process parameters and conditions, exploring multi-layer depositions. This involves refining the PL intervals to represent varying levels of variability and tuning the ML models to improve generalisation. Additionally, although machine learning enables rapid modelling of deposited material behaviour, it is important to maintain the connection to the physical significance of welding conditions. To support this, data augmentation using validated ML models can be a useful method for evaluating different hypotheses and formulations regarding material behaviour.

Author contribution Carlos Zhu: writing—original draft, visualization, validation, methodology, investigation, formal analysis, writing—review and editing. Trayana Tankova: conceptualization, formal analysis, methodology, supervision, validation, writing—review and editing. Amin S. Azar: conceptualization, formal analysis, methodology, supervision, validation, writing—review and editing. Ricardo Branco: conceptualization, investigation, methodology, supervision, validation, writing—review and editing. Luís Simões da Silva: conceptualization, investigation, methodology, supervision, validation, writing—review and editing.

Funding Open access funding provided by FCT|FCCN (b-on). This work was partly financed by (1) FCT/MCTES through national funds (PIDDAC) under the R&D Unit Institute for Sustainability and Innovation in Structural Engineering (ISISE), under reference UIDB/04029/2020 (https://doi.org/10.54499/UIDB/04029/2020), and under the Associate Laboratory Advanced Production and Intelligent Systems (ARISE) under reference LA/P/0112/2020. (2) CEMMPRE projects under the references UIDB/00285/2020 and LA/P/0112/2020. (3) The doctoral grant 2021.05992.BD by the Portuguese Foundation for Science and Technology (FCT) attributed to the first author (https://doi.org/10.54499/2021.05992.BD). (4) The AMCONSTRUCTION project, which is part of the UCPATRONAGE 2019 initiative and a joint effort between CEMMPRE (R&D Unit, The Centre for Mechanical Engineering, Materials and Processes) and ISISE (R&D Unit Institute for Sustainability and Innovation in Structural Engineering). (5) The Research Fund for Coal and Steel under grant agreement 101112614 (IAMFat). (6) ROBIN project granted under ARISE Support Programme with sub-grant agreement ARISE_1OC_8.

Declarations

Competing interests The authors declare no competing interests.

References

1. ASTM, Wohlers Report 2023 Unveils Continued Double-Digit Growth.[Online]. Available: https://wohlersassociates.com/news/wohlers-report-2023-unveils-continued-double-digit-growth/ Accessed: 07 Oct 2024
2. Tofail SAM, Koumoulos EP, Bandyopadhyay A, Bose S, O'Donoghue L, Charitidis C (2018) Additive manufacturing: scientific and technological challenges, market uptake and opportunities. Mater Today 21(1):22–37. https://doi.org/10.1016/j.mattod.2017.07.001

3. Chen Z, Han C, Gao M, Kandukuri SY, Zhou K (2022) A review on qualification and certification for metal additive manufacturing. Virtual Phys Prototyp 17(2):382–405. https://doi.org/10.1080/17452759.2021.2018938
4. Srivastava S, Garg RK, Sharma VS, Sachdeva A (2021) Measurement and mitigation of residual stress in wire-arc additive manufacturing: a review of macro-scale continuum modelling approach. Arch Comput Methods Eng 28(5):3491–3515. https://doi.org/10.1007/s11831-020-09511-4
5. Evans SI, Wang J, Qin J, He Y, Shepherd P, Ding J (2022) A review of WAAM for steel construction – manufacturing, material and geometric properties, design, and future directions. Structures 44:1506–1522. https://doi.org/10.1016/j.istruc.2022.08.084
6. Le VT et al (2022) Prediction and optimization of processing parameters in wire and arc-based additively manufacturing of 316L stainless steel. J Braz Soc Mech Sci Eng 44(9):394. https://doi.org/10.1007/s40430-022-03698-2
7. Karmuhilan M, Sood AK (2018) Intelligent process model for bead geometry prediction in WAAM. Mater Today Proc 5(11):24005–24013. https://doi.org/10.1016/j.matpr.2018.10.193
8. Wang Z, Zimmer-Chevret S, Léonard F, Abba G (2021) Prediction of bead geometry with consideration of interlayer temperature effect for CMT-based wire-arc additive manufacturing. Weld World 65(12):2255–2266. https://doi.org/10.1007/s40194-021-01192-2
9. Tomar B, Shiva S, Nath T (2022) A review on wire arc additive manufacturing: processing parameters, defects, quality improvement and recent advances. Mater Today Commun 31:103739. https://doi.org/10.1016/j.mtcomm.2022.103739
10. Azar AS (2025) A method and system for determining and monitoring automated additive manufacturing process parameters. EP4566746A1. https://patents.google.com/patent/EP4566746A1/en. Accessed Aug 2025
11. Rosli NA, Alkahari MR, Abdollah MFB, Maidin S, Ramli FR, Herawan SG (2021) Review on effect of heat input for wire arc additive manufacturing process. J Market Res 11:2127–2145. https://doi.org/10.1016/j.jmrt.2021.02.002
12. Mondal A, Saha MK, Hazra R, Das S (2016) Influence of heat input on weld bead geometry using duplex stainless steel wire electrode on low alloy steel specimens. Cogent Eng 3(1):1143598. https://doi.org/10.1080/23311916.2016.1143598
13. Khrais S, Al Hmoud H, Abdel Al A, Darabseh T (2023) Impact of gas metal arc welding parameters on bead geometry and material distortion of AISI 316L. JMMP 7(4):123. https://doi.org/10.3390/jmmp7040123
14. Yildiz AS, Davut K, Koc B, Yilmaz O (2020) Wire arc additive manufacturing of high-strength low alloy steels: study of process parameters and their influence on the bead geometry and mechanical characteristics. Int J Adv Manuf Technol 108(11–12):3391–3404. https://doi.org/10.1007/s00170-020-05482-9
15. Gudur S, Nagallapati V, Pawar S, Muvvala G, Simhambhatla S (2021) A study on the effect of substrate heating and cooling on bead geometry in wire arc additive manufacturing and its correlation with cooling rate. Mater Today Proc 41:431–436. https://doi.org/10.1016/j.matpr.2020.10.071
16. Ščetinec A, Klobčar D, Bračun D (2021) In-process path replanning and online layer height control through deposition arc current for gas metal arc based additive manufacturing. J Manuf Process 64:1169–1179. https://doi.org/10.1016/j.jmapro.2021.02.038
17. Almeida P (2012) Process control and development in wire and arc additive manufacturing. PhD Thesis, Cranfield University. [Online]. Available: http://dspace.lib.cranfield.ac.uk/handle/1826/7845. Accessed: 07 Oct 2024
18. Pires JN, Azar AS, Nogueira F, Zhu CY, Branco R, Tankova T (2022) The role of robotics in additive manufacturing: review of the AM processes and introduction of an intelligent system. IR 49(2):311–331. https://doi.org/10.1108/IR-06-2021-0110
19. Chan B, Pacey J, Bibby M (1999) Modelling gas metal arc weld geometry using artificial neural network technology. Can Metall Q 38(1):43–51. https://doi.org/10.1179/cmq.1999.38.1.43
20. Xiong J, Zhang G, Hu J, Wu L (2014) Bead geometry prediction for robotic GMAW-based rapid manufacturing through a neural network and a second-order regression analysis. J Intell Manuf 25(1):157–163. https://doi.org/10.1007/s10845-012-0682-1
21. Nalajam PK, Varadarajan R (2021) Experimental and theoretical investigations on cold metal transfer welds using neural networks: a computational model of weld geometry. Exp Tech 45(6):705–720. https://doi.org/10.1007/s40799-021-00451-7
22. Petrik J, Sydow B, Bambach M (2022) Beyond parabolic weld bead models: AI-based 3D reconstruction of weld beads under transient conditions in wire-arc additive manufacturing. J Mater Process Technol 302:117457. https://doi.org/10.1016/j.jmatprotec.2021.117457
23. Banaee SA, Kapil A, Marefat F, Sharma A (2023) Generalised overlapping model for multi-material wire arc additive manufacturing (WAAM). Virtual Phys Prototyp 18(1):e2210541. https://doi.org/10.1080/17452759.2023.2210541
24. Ding D, Pan Z, Cuiuri D, Li H (2015) A multi-bead overlapping model for robotic wire and arc additive manufacturing (WAAM). Robot Comput-Integr Manuf 31:101–110. https://doi.org/10.1016/j.rcim.2014.08.008
25. Mattera G, Nele L, Paolella D (2024) Monitoring and control the wire arc additive manufacturing process using artificial intelligence techniques: a review. J Intell Manuf 35(2):467–497. https://doi.org/10.1007/s10845-023-02085-5
26. Lettori J, Esposto C, Peruzzini M, Pellicciari M, Raffaeli R (2025) Geometrical characterization of circular multi-layered CMT WAAM specimens by 3D structured light scanning. Int J Adv Manuf Technol 136(11–12):5305–5334. https://doi.org/10.1007/s00170-025-15107-8
27. Fronius International, 'TPS/i WireSense: the welding wire as sensor', 2020. [Online]. Available:https://www.fronius.com/en/welding-technology/info-centre/magazine/2020/tpsi-wire-sense Accessed: 07 Oct 2024
28. Prasad RK, Sarmah R,Chakraborty S (2019) Incremental k-means method', in pattern recognition and machine intelligence vol 11941. In: Deka B, Maji P, Mitra S, Bhattacharyya DK, Bora PK, Pal SK (eds) Lecture Notes in Computer Science. Cham: Springer International Publishing, pp 38–46. https://doi.org/10.1007/978-3-030-34869-4_5
29. Fischler MA, Bolles RC (1981) Random sample consensus: a paradigm for model fitting with applications to image analysis and automated cartography. Commun ACM 24(6):381–395. https://doi.org/10.1145/358669.358692
30. Ester M, Kriegel H-P, Sander J, Xu X (1996) A density-based algorithm for discovering clusters in large spatial databases with noise. In: Knowledge Discovery and Data Mining. [Online]. Available: https://api.semanticscholar.org/CorpusID:355163. Accessed Oct 2024
31. Bellock KE (2021) Alpha Shape Toolbox. [Online]. Available: https://pypi.org/project/alphashape/. Accessed 07 Oct 2024
32. Felkel P, Alek SEAOZ (1998) Straight skeleton implementation. [Online]. Available: https://api.semanticscholar.org/CorpusID:14744149. Accessed Oct 2024

33. Tankova T, Andrade D, Branco R, Zhu C, Rodrigues D, Simões da Silva L (2022) Characterization of robotized CMT-WAAM carbon steel. J Constr Steel Res 199:107624. https://doi.org/10.1016/j.jcsr.2022.107624
34. Feng Y, Fan D (2024) Investigating the forming characteristics of 316 stainless steel fabricated through cold metal transfer (CMT) wire and arc additive manufacturing. Materials 17(10):2184. https://doi.org/10.3390/ma17102184
35. Catalano AR, Tebaldo V, Priarone PC, Settineri L, Faga MG (2025) Cmt deposition of stainless steel: effects of process parameters on energy demand and microstructure. Prog Addit Manuf. https://doi.org/10.1007/s40964-025-01022-7
36. Mohd Mansor MS et al (2024) Integrated approach to wire arc additive manufacturing (WAAM) optimization: harnessing the synergy of process parameters and deposition strategies. J Mater Res Technol 30:2478–2499. https://doi.org/10.1016/j.jmrt.2024.03.170
37. Williams S, Gitto E, Jared B (2024) Interpass temperature impact on bead geometry of mild steel in wire-arc additive manufacturing. Manuf Lett 41:992–997. https://doi.org/10.1016/j.mfglet.2024.09.123
38. Ibrahim IA, Mohamat SA, Amir A, Ghalib A (2012) The effect of gas metal arc welding (GMAW) processes on different welding parameters. Procedia Eng 41:1502–1506. https://doi.org/10.1016/j.proeng.2012.07.342
39. Lambiase F, Scipioni SI, Paoletti A (2022) Accurate prediction of the bead geometry in wire arc additive manufacturing process. Int J Adv Manuf Technol 119(11–12):7629–7639. https://doi.org/10.1007/s00170-021-08588-w
40. Norrish J, Polden J, Richardson I (2021) A review of wire arc additive manufacturing: development, principles, process physics, implementation and current status. J Phys D Appl Phys 54(47):473001. https://doi.org/10.1088/1361-6463/ac1e4a